Energy 159 (2018) 961–976

Contents lists available at ScienceDirect

Energy

journal homepage: www.elsevier.com/locate/energy

Darrieus wind turbine prototype: Dynamic modeling parameter identification and control analysis

T.R. Pereira [a], N.C. Batista [a, b], A.R.A. Fonseca [a], C. Cardeira [a], P. Oliveira [a], R. Melicio [a, b, c, *]

[a] IDMEC, Instituto Superior Técnico, Universidade de Lisboa, Portugal
[b] ICT, Universidade de Évora, Portugal
[c] Departamento de Física, Escola de Ciências e Tecnologia, Universidade de Évora, Portugal

ARTICLE INFO

Article history:
Received 15 April 2018
Received in revised form
4 June 2018
Accepted 24 June 2018
Available online 29 June 2018

Keywords:
Wind energy
Darrieus wind turbines
Prototype
Dynamic modeling
System identification
Control analysis
LQR controller

ABSTRACT

This paper details the process required to develop a linear dynamic model and control of a Darrieus wind turbine equipped with a Permanent Magnet Synchronous Generator. The turbine is to be integrated in a smart grid for future installation in urban context. An active control system is integrated in such a way that, even in the presence of non-ideal phenomena and disturbances, optimal operation is achieved. For the class of linear (or linearized) systems such optimal control solution corresponds to the Linear Quadratic Regulator (LQR). A set of tests were performed on a wind tunnel, data was acquired allowing the application of well rooted identification techniques, leading to the deduction and validation of several low order dynamic models. Optimal control solutions were implemented to guarantee that close to ideal operational conditions are maintained. As such, efficiency is improved without jeopardizing the integrity of the wind turbine in a broad set of operational conditions.

1. Introduction

Recently, renewable energy has significantly increased its market penetration in power production [1]. Conversion of wind energy to electric energy is considered one of the most economically advantageous conversions [2]. This interesting conversion of energy is one of many reasons why lately wind power systems have been receiving significant investments and have been the focus of intense research [3]. This rise has been accompanied with the awareness that fossil fueled based energy use results in high quantity emissions of CO_2 [4,5]. Also, in the future energy system, decentralized power production grows in importance, for local power production integrated in smart grids [7].

The share of renewable energy in the global power production has clearly increased. However, the fact that these are fluctuating resources, creating an unbalance between supply and demand, requires an effort in maximizing and stabilizing power production, leading to the creation of control strategies in order to improve the technology itself towards its integration in a smart energy grid context.

Presently the primary technology used in wind power generation consists in Horizontal Axis Wind Turbines (HAWT) [8]. However the HAWT technology is inappropriate on urban context given the negative visual impact, noise pollution and inability to quickly adapt to fast wind changes present in urban areas. Moreover the independence of the wind direction in a VAWT is a big advantage against HAWT. A solution to generate energy from wind closer to the consumer and to increase the wind power usage is the Darrieus Vertical Axis Wind Turbine (VAWT) technology. The Darrieus is driven by lift force, while the Savonius VAWT works through drag force, which makes the Darrieus more efficient. These types of systems have recently received growing interest for energy harvesting purposes in the urban environment [7–14]. In comparison to HAWT, most VAWT models have the following advantages [4,5]:

- Performance is independent from wind direction, thus not requiring any special mechanisms for yawing into wind, VAWT have the ability to generate energy from wind skewed flows;
- Smaller number of components;
- Lower noise;

* Corresponding author. IDMEC, Instituto Superior Técnico, Universidade de Lisboa, Portugal.
E-mail address: ruimelicio@gmail.com (R. Melicio).

https://doi.org/10.1016/j.energy.2018.06.162
0360-5442/

- Blades can be manufactured by mass production extrusion, since they are often untwisted and of constant chord;
- Ability to operate closer to the ground with the generator usually installed on the base, offering simpler and cheaper maintenance.

A VAWT is classified into three technological types: Savonius, Darrieus and H-Rotor see Ref. [16] for details. In this paper the prototype developed in Refs. [4–7] and in the references therein, is a curved bladed Darrieus VAWT with self-start for wind speeds of 1.25 m/s. The interest in this type of VAWT is due to the ability to spin faster than the incoming wind speed. Unlike the Savonius VAWT, the Darrieus wind turbine is a high speed, low torque machine, usually requiring a startup force to initiate its operation, that is, the lack of binary has to be conveniently tackled. The Darrieus type is experiencing a growth in development and installation as a result of the interest for decentralizing electric energy sources located in urban areas [4].

In Ref. [6] a self-start Darrieus wind turbine prototype for urban context was developed, where the innovative design avoids the need for extra components and external electric energy feed-in. This work is a follow-up of that research line of that work and profits from the data available therein. A dynamic model for the HAWT system can be found in Ref. [9], with similar purposes as the work reported on the present work, i.e. the equations required to model the Permanent Magnet Synchronous Generator (PMSG) are presented in detail, complemented with the theory behind the machine.

Different control strategies are reported in Ref. [11]. A performance comparison and evaluation for a two mass dynamic model was developed for a HAWT equipped with an induction generator. In Ref. [12] general equations for modeling a VAWT equipped with a synchronous generator are detailed. In Ref. [13] a study is presented for modeling and design of an wind energy conversion systems (WECS), using a wind turbine with known dynamic characteristics and PMSG with a back to back power converter topology. System identification techniques for nonlinear systems can be found in Ref. [15], similar to the ones to be applied in this work.

In Ref. [16] the research of the power production of two small-size commercial wind turbines, with both horizontal and vertical axis, characterized by the same rated power of 20 kW, installed in the Savona Harbour is performed. An interesting conclusion is that the VAWT presents a higher quality solution for urban integration. In Ref. [18] all necessary equations required for modeling the PMSG are derived. The generator model is established in the synchronous rotating reference frame.

Classical AutoRegressive-Moving-Average (ARMA) identification techniques are used for identifying the model. Different strategies could used for control like PID or Lead-Lag. However, these techniques do not have stability proves, in general. For linear systems it is proven that the LQR guarantees stability and optimality [17].

This paper proposes a structured method to derive linear models for the non linear general model of the VAWT prototype. Furthermore, it is complemented with a experimental setup and analysis for parameter identification. The correct identification of the model and its parameters paves the way to reliable and powerful control strategies. In what concerns to the model proposed, it is based on first physics principles so it is our believe that the model scales well for larger wind turbines, while phenomena of rigidity and aero-elasticity holds, given appropriate identification procedures. It is important to remark that our design is for urban context, so very large models are out of scope.

The paper is organized as follows: Section 2 presents the VAWT dynamic modeling; the drive-train and PMSG dynamic models; the linearizations performed; the state space model and the moment of inertia model. Section 3 presents the frequency analysis and the second-order model. Section 4 presents the experimental setup, namely the inertial moment determination; the single input single output identification; the experimental data and parameters identification. Finally, concluding remarks are given in Section 5.

2. Modeling

2.1. VAWT dynamic model

The VAWT dynamics is modeled taking into account the assumption that all particles present in the wind are moving at a constant speed and direction.

For HAWT the Tip Speed Ratio (TSR) is defined by the quotient between the tangential linear speed of the rotor at the tip of the blade and the wind speed, that is perpendicular to the swept area of the blades. For the VAWT the TSR is more complicated since there are two tips of the blade and depending on their design the tips can be closer or farther to the rotating axis. Since for the VAWT turbine considered the tips are closer to the rotating axis than the middle section of the blade, the tip speed ratio will be calculated at middle height of the turbine.

The aerodynamic power captured by the VAWT rotor P_a [19] is given by:

$$P_a = \rho r H\, C_p(\lambda)\, \nu^3 = \omega\, T_a \tag{1}$$

where ρ is the air density, r is the turbine radius, H is the turbine height, $C_p(\lambda)$ is the power coefficient as function of λ, λ is the TSR, ν is the wind speed, ω is the turbine rotor angular speed and T_a is the aerodynamic torque.

The aerodynamic torque T_a is given by:

$$T_a = \rho r^2 H C_p(\lambda) \nu^2 \frac{1}{\lambda} \tag{2}$$

Details about these formulas can be found in Ref. [19].

Previous studies and simulations [6] have achieved a practical relation between C_p and λ, shown in Fig. 1.

A 2^{nd} order polynomial that analytically describes the behavior of C_p with the TSR. C_p is applied to (1), leading to:

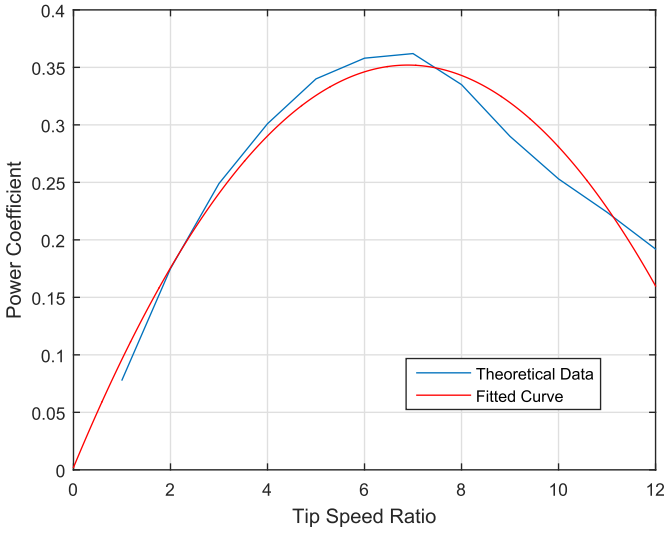

Fig. 1. C_p Vs TSR(λ).

$$P_a = \rho r H\Big(-0.007365\lambda^2 + 0.1015\lambda + 0.002052\Big)v^3 \quad (3)$$

The non linear aerodynamic torque is given by:

$$T_a(v,\omega) = \rho r H\Big(-0.007365\lambda^2 + 0.1015\lambda + 0.002052\Big)\, v^3\, \omega^{-1} \quad (4)$$

2.2. Drive-train and PMSG dynamic models

The drive-train dynamics is simplified and represented as a torsion system with discretization of masses. To calculate the applied aerodynamic torque, some assumptions for the motion of the drive-train are required: the rotor is assumed to act as a rigid body and therefore, to have the same acceleration over the entire axis of rotation; aerodynamic effects are integrated over the length of the blade and summed up for all the blades.

Applying the rotational version of Euler's law:

$$J_t\, \dot{\omega} = T_a - T_{em} - \beta\, \omega \quad (5)$$

where J_t is the total inertial moment of the VAWT, T_a is the aerodynamic torque, T_{em} is the measured electromagnetic torque, and β is the damping coefficient.

This turbine is small enough to neglect the mechanical vibrations.

The PMSG model used is presented in Refs. [9,10]. In order to apply a control strategy that uses, as actuation, a variable load resistance, the closed circuit resistive load R is given by:

$$R = R_a + R_c \quad (6)$$

where R_a is the armature resistance and R_c the load resistance that will be the variable to control.

The electromagnetic torque is given by:

$$T_{em} = \frac{3}{2} n_p \left((L_d - L_q) i_d i_q + i_q \lambda_o\right) \quad (7)$$

Considering the PMSG model [9], the coil inductances $L_d = L_q = L$. Hence, the electromagnetic torque is given by:

$$T_{em} = \frac{3}{2} n_p \lambda_o i_q \quad (8)$$

Preliminary tests performed on the PMSG were developed in order to obtain a relation between the generator voltage and the angular rotor speed. Two of those tests were performed with the generator in open and short circuit, with results shown in Fig. 2a and in Fig. 2b. Voltage varies linearly with angular speed according to (9) and (10).

$$U(\omega) = 0.2841\, \omega + 0.2193\ (V) \quad (9)$$

$$I(\omega) = 0.0089\, \omega - 0.0004\ (A) \quad (10)$$

The referential transform from the three phase system (*123*) referential to the simplified (*dq*) referential, corresponds to a positive gain:

$$u_q = 1.5\sqrt{\frac{2}{3}}\, U \text{ and } i_q = 1.5\sqrt{\frac{2}{3}}\, I \quad (11)$$

Using the PMSG model [9] and (9) and (10), the state space representation variables can be replaced by direct relations to the angular speed of the turbine. The modified state space is given by:

$$\frac{di_q}{dt} = -\frac{R}{L} 1.2247\ (0.0089\, \omega - 0.0004) - n_p\, \omega\, \frac{\lambda_o}{L} + \frac{1}{L} 1.2247\ (0.2841\, \omega + 0.2193) \quad (12)$$

$$\frac{di_d}{dt} = 0 \quad (13)$$

2.3. Linear model

The dynamic linear model of the drive-train is based on first principles of physics and circuits. It is very difficult or even impossible to have tests for each parameter isolated. Thus the model is deduced and identification tools were used, resorting to wind tunnel tests, to obtain the coefficients of the transfer functions (TF) deduced from the model, when Laplace transform is used.

The linearization of the aerodynamic torque due to wind impact on the blades, resorts to the Taylor series expansion and is given by:

$$T_a(v,\omega) \approx \overline{T_a} + a\, \delta v + b\, \delta\omega \quad (14)$$

where $\delta v = v - \bar{v}$, $\delta\omega = \omega - \overline{\omega}$ and a and b are given by:

$$a = \frac{\partial T_a}{\partial v}|_{opt} \quad b = \frac{\partial T_a}{\partial \omega}|_{opt} \quad (15)$$

where, *opt* is the parameter values where the linearization is being performed, namely wind speed and angular speed.

Linearizing (12) and (13) around a generic operating point, the linearized equations are given by:

$$\delta \dot{i_q} \approx c\, \delta R_c + d\, \delta\omega \quad (16)$$

$$\delta \dot{i_d} \approx 0 \quad (17)$$

where $\delta \dot{i_q} = \dot{i_q} - \overline{\dot{i_q}}$, $\delta \dot{i_d} = \dot{i_d} - \overline{\dot{i_d}}$, $\delta R_c = R_c - \overline{R_c}$ and c, d, g, j and k are given by:

$$c = \frac{\partial \dot{i_q}}{\partial R_c}|_{opt} \quad d = \frac{\partial \dot{i_q}}{\partial \omega}|_{opt} \quad (18)$$

Linearizing around an operating point, the electromagnetic torque expressed in equation (7) is given by:

$$T_{em} \approx \overline{T_{em}} + e\, \delta i_q \quad (19)$$

where $\delta i_q = i_q - \overline{i_q}$ and e is given by:

$$e = \frac{\partial T_{em}}{\partial i_q}|_{opt} \quad (20)$$

For a control strategy it is important to merge (5) with the linearized quantities of interest.

Merging (14) and (19) in (5), a linear relation is achieved:

$$\delta\dot{\omega} \approx \frac{1}{J_t}\left(\overline{T_a} + a\, \delta v + b\, \delta\omega - \overline{T_{em}} - e\, \delta i_q - \beta(\delta\omega + \overline{\omega})\right) \quad (21)$$

Applying Laplace transform:

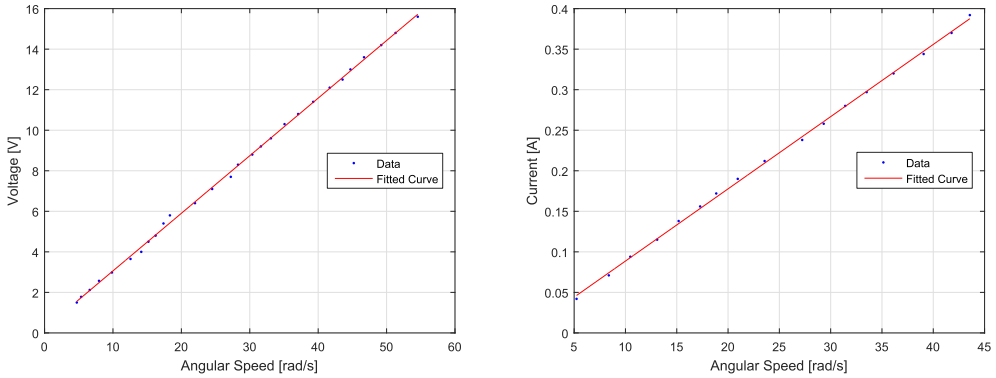

(a) (b)

Fig. 2. a) Open circuit analysis: Voltage vs angular speed. b) Short circuit analysis: Current vs angular speed.

$$s\,\Delta\omega(s) \approx \frac{1}{J_t}\left(\overline{T_a} + a\,\Delta v(s) + b\,\Delta\omega(s) - \overline{T_{em}} - e\,\Delta i_q(s) - \beta\Delta\omega(s) - \beta\overline{\omega}\right) \tag{22}$$

where a, b and e are given by:

$$a = \frac{\partial T_a}{\partial v}|_{opt} \quad b = \frac{\partial T_a}{\partial \omega}|_{opt} \tag{23}$$

$$e = \frac{\partial T_{em}}{\partial i_q}|_{opt} = \frac{3}{2}\,n_p\,\lambda_o \tag{24}$$

Considering $\overline{T_{em}} = \overline{T_a} - \beta\,\overline{\omega}$ and $\beta = 0$ the following simplification is obtained:

$$\delta\dot{\omega} \approx \frac{1}{J_t}\left(a\,\delta v + b\,\delta\omega - e\,\delta i_q\right) \tag{25}$$

The closed loop model with the controller is shown in Fig. 3 where the control variable is δR_c.

Two distinct transfer functions can be analyzed, one for each input. The second order approach is given by:

$$TF1^2 = \frac{\Delta\omega(s)}{\Delta v(s)} = \frac{a\,s}{J_t\,s^2 - b\,s + e\,d} \tag{26}$$

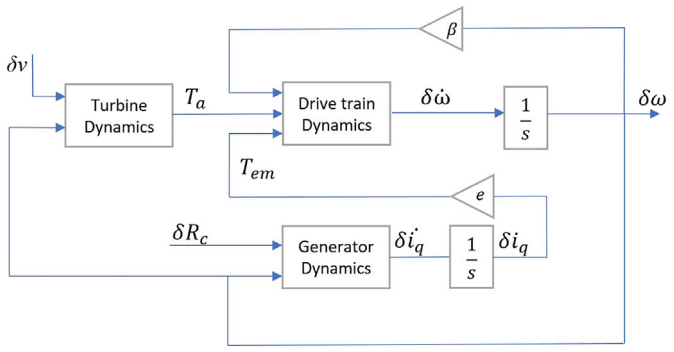

Fig. 3. Linear model scheme with controller.

$$TF2^2 = \frac{\Delta\omega(s)}{\Delta R_c(s)} = \frac{-e\,c}{J_t\,s^2 - b\,s + e\,d} \tag{27}$$

where $TF1^n$ is the transfer function of an nth order model from the wind speed variation input to the angular speed variation output and $TF2^n$ is the transfer function of an nth order model from the circuit resistance variation input to the angular speed variation output.

For numerical analysis Table 1 is presented, containing physical specifications of the prototype and the PMSG and numerical data retrieved from the linearized equations.

2.4. State space model

In order to obtain a state space representation, and taking into account the dynamic modeling done previously, the state variables chosen are $\delta\omega$ and δi_q, using the state vector $\mathbf{x} = \left[\delta\omega \quad \delta i_q\right]^T$ and the

Table 1
Case Study Specifications and linearization constants.

Parameters	Symbol	Value
Nominal Wind Speed (m/s)	$\overline{v}$	6
Nominal Angular Speed (rad/s)	$\overline{\omega}$	239.0658
Nominal Current (mA)	$\overline{i_q}$	11.2
Nominal Load Resistance (Ω)	$\overline{R_c}$	136.6
Nominal Output Power(W)	$\overline{P_{out}}$	6.4955
Radius (m)	r	0.173
Height (m)	H	0.48
N of Blades	Z	5
Blade body (m)	–	0.36
Airfoil chord (m)	–	0.053
Airfoil weight (g)	–	180
Generator type	–	3 phase AC
Rated Voltage (V)	–	16
Rated Power (W)	–	15
N of poles	n_p	6
Stator resistance (Ω)	R_a	4.3
PM Flux Linkage (Wbturns)	λ_o	0.272
Inductance (mH)	L	40
Motor Inertia (kg m^2)	–	0.000179
a	–	0.0138
b	–	-1.1507×10^{-4}
c	–	− 35.478
d	–	− 0.0109
e	–	2.448

output vector $\mathbf{y} = [\delta\omega]$, it is possible to infer that the state space representative of the system is given by:

$$\begin{cases} \dot{\mathbf{x}}(t) = \mathbf{A}\mathbf{x}(t) + \mathbf{B}\,\mathbf{u}(t) + \mathbf{E}\,\delta\mathbf{v}(t) \\ \dot{\mathbf{y}}(t) = \mathbf{C}\mathbf{x}(t) + \mathbf{D}\mathbf{u}(t) \end{cases} \tag{28}$$

where δv is the disturbance and $\mathbf{u} = \delta R_c$, $\mathbf{A}$, $\mathbf{B}$, $\mathbf{C}$ and $\mathbf{E}$ are given by:

$$\mathbf{A} = \begin{bmatrix} b\,J^{-1} & -e\,J^{-1} \\ d & 0 \end{bmatrix}, \quad \mathbf{B} = \begin{bmatrix} 0 \\ c \end{bmatrix}, \quad \mathbf{E} = \begin{bmatrix} a\,J^{-1} \\ 0 \end{bmatrix} \tag{29}$$

$$\mathbf{C} = [1 \quad 0], \quad \mathbf{D} = [0] \tag{30}$$

2.5. Moment of inertia

The knowledge of the inertia moment is important to develop and simulate control strategies for the VAWT prototype shown in Fig. 4. A precise analysis of the inertia moment would take into account the static and dynamic friction as well as the inertia moments of the parts involved in the measurement system, or some frictionless approaches might be made. Moreover, the inertia moment can be theoretically computed from the CAD model of the VAWT prototype. Both calculations have to give a similar result.

The inertia moment is a constant that is strictly implied to the dynamics of the system. Therefore, the following experiment was performed in order to determine the total inertial moment J_t. For a easy understanding of the variables in hand a scheme is shown in Fig. 5.

In Fig. 5 H is the turbine height, d is the turbine diameter, y is the predefined distance, a is the linear acceleration, g is the gravity.

In order to determine the total inertial moment, if the body shape does not change, which is the case, the inertia moment appears in Newton's law of motion as the ratio of an applied torque ($\vec{\tau}$) on a body to the angular acceleration ($\vec{\alpha}$) around a principal axis, given by:

$$J_t = \frac{\vec{\tau}}{\vec{\alpha}} \tag{31}$$

The angular acceleration is given by:

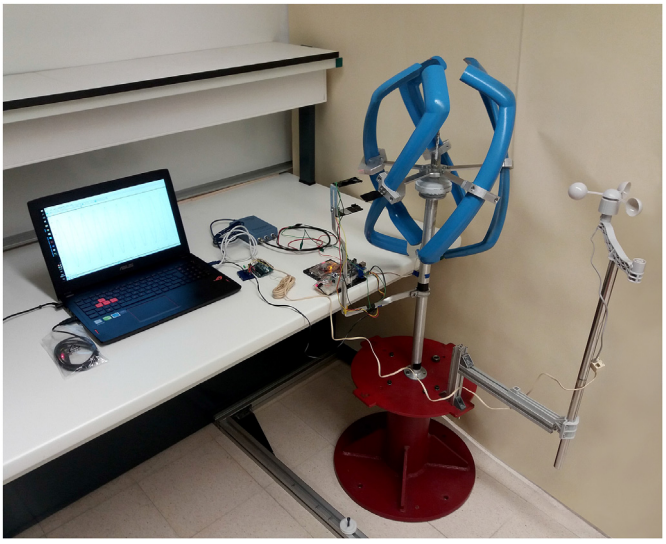

Fig. 4. Prototype and sensors.

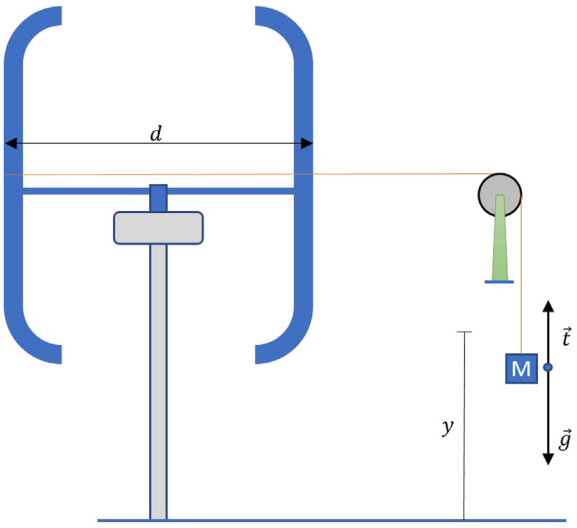

Fig. 5. Inertial moment experiment assembly.

$$\vec{\alpha} = \frac{4\,y}{d\,t^2} \tag{32}$$

where t is the time interval considered.

From the motion equations the distance y is given by:

$$y = \frac{a\,t^2}{2} \tag{33}$$

The torque ($\vec{\tau}$) acting on the axle in function of the tension applied by the wire on the turbine structure T is given by:

$$\vec{\tau} = T\,\frac{d}{2} = \left(M\,g - M\,\frac{2y}{t^2}\right)\,\frac{d}{2} \tag{34}$$

The inertial moment J_t is given by:

$$J_t = \frac{M\,g\,d^2\,t^2}{8\,y} - \frac{M\,d^2}{4} \quad \left(\mathrm{kg\,m^2}\right) \tag{35}$$

3. Control analysis

3.1. Second order model

A simplified set of equations describing the TF between both inputs and the output is given by:

$$TF1^2 = \frac{\Delta\omega(s)}{\Delta v(s)} = \frac{a\,s}{J_t\,s^2 - b\,s + e\,d} \tag{36}$$

$$TF2^2 = \frac{\Delta\omega(s)}{\Delta R_c(s)} = \frac{-e\,c}{J_t\,s^2 - b\,s + e\,d} \tag{37}$$

This set of equations is used throughout the control strategy analysis.

To control the Power output, which is ultimately the variable of interest, a torque control scheme can be used to regulate the power by controlling the generator active current, which as demonstrated previously, has a linear relationship with the electromagnetic torque. The output power is determined by the following equation:

$$P_{out} = 1.5 n_p \lambda_o i_q \omega - R i_q^2 \tag{38}$$

where R is given by equation (6).

Linearizing (38) the output power is given by:

$$P_{out} \approx 1.5 n_p \lambda_o \overline{i_q} \Delta\omega + \left(1.5 \lambda_o \overline{\omega} - 2R\overline{i_q}\right)\Delta i_q + \overline{P_{out}} \tag{39}$$

In order to obtain the TF for the output power according to the generator active current the following methodology is applied. From (5) it is possible to retrieve the following TF:

$$\frac{\Delta\omega(s)}{\Delta i_q(s)} \approx \frac{1.5\ n_p\ \lambda_o}{s - \frac{1}{J_t} b + \frac{\beta}{J_t}} \tag{40}$$

where the incorporation in the first term of (39) allows the development of a TF relating both variables of interest, given by:

$$\frac{\Delta P_{out}(s)}{\Delta i_q(s)} \approx \left(1.5 n_p \lambda_o \overline{\omega} - 2R\overline{i_q}\right) - \frac{\overline{i_q}\left(1.5 n_p \lambda_0\right)^2}{s - \frac{1}{J_t} b + \frac{\beta}{J_t}} \tag{41}$$

Simplifying:

$$\frac{\Delta P_{out}(s)}{\Delta i_q(s)} \approx \left(1.5 n_p \lambda_o \overline{\omega} - 2R\overline{i_q}\right) \frac{s - \left(\frac{1}{J_t} b - \frac{\beta}{J} + \frac{\overline{i_q}\left(1.5 n_p \lambda_0\right)^2}{\left(1.5 n_p^2 \lambda_o \overline{\omega} - 2R\overline{i_q}\right)}\right)}{s - \frac{1}{J_t} b + \frac{\beta}{J_t}} \tag{42}$$

The general TF that has as output the generated power and input the angular speed is given by:

$$\frac{\Delta P_{out}(s)}{\Delta\omega(s)} \approx \frac{\Delta P_{out}}{\Delta i_q} \left(\frac{\Delta\omega}{\Delta i_q}\right)^{-1} \tag{43}$$

$$\frac{\Delta P_{out}(s)}{\Delta\omega(s)} \approx \left(1.5 n_p \lambda_o \overline{\omega} - 2R\overline{i_q}\right) \frac{s - \left(\frac{1}{J_t}\ b - \frac{\beta}{J_t} + \frac{\overline{i_q}\left(1.5 n_p \lambda_0\right)^2}{\left(1.5 n_p^2 \lambda_o \overline{\omega} - 2R\overline{i_q}\right)}\right)}{s - \frac{1}{J_t}\ b + \frac{\beta}{J_t}} \left(-\frac{1.5 n_p \lambda_o}{s - \frac{1}{J_t}\ b + \frac{\beta}{J_t}}\right)^{-1} \tag{44}$$

Simplifying:

$$\frac{\Delta P_{out}(s)}{\Delta\omega(s)} \approx -\frac{J_t\left(1.5 n_p \lambda_o \overline{\omega} - 2R\overline{i_q}\right)}{1.5 n_p \lambda_o} \left[s - \left(\frac{1}{J_t}\ b - \frac{\beta}{J_t} + \frac{\overline{i_q}\left(1.5 n_p \lambda_0\right)^2}{\left(1.5 n_p \lambda_o \overline{\omega} - 2R\overline{i_q}\right)}\right)\right] \tag{45}$$

To study the stability a *Root Locus* analysis is performed. To characterize the frequency response a *Bode* analysis is presented.

Until now, the equations are presented with variables. The following analysis is performed for Case Study 1, shown in Fig. 6. For the second order model neglecting the damping coefficient ($\beta \approx 0$), $TF2^2$ (37) is given by:

$$TF2^2 = \frac{\Delta\ \omega(s)}{\Delta R_c(s)} = \frac{868.9}{s^2\ + 1.1507 \times 10^{-3} s - 0.4} \tag{46}$$

By the *Root Locus* analysis it is clear that the system is marginally stable, that is, for $K = 0$ it is unstable, however for $K > 0.00046$ the system becomes stable. Therefore it is required to use a controller a gain higher than 0.00046.

3.2. System characterization in open loop

Considering the seconder order model state space representation as shown in (28)–(30) the following system characterization was performed:

3.2.1. Controllability

Computing the state controllability matrix, given by:

$$\mathbf{C_s} = \begin{bmatrix} 0 & a J^{-1} & -e\, c J^{-1} & b\, a J^{-2} \\ c & 0 & 0 & d\, a J^{-1} \end{bmatrix} \tag{47}$$

From this analysis, it can be stated that the system is completely state controllable (for nonzero parameters) since the vectors $\mathbf{B}, \mathbf{AB}, \ldots, \mathbf{A^{n-1}B}$ are linearly independent which is the same that having the controllability matrix of *rank* $= n = 2$.

3.2.2. Observability

Computing the state observability matrix, given by:

$$\mathbf{O} = \begin{bmatrix} 1 & 0 & -b J^{-1} & d \\ 0 & 1 & -e J^{-1} & 0 \end{bmatrix} \tag{48}$$

For the observability the rank of the matrix is 2. Hence, the system is completely observable.

3.2.3. Stability

Regarding stability of the system, by resorting to the Lyapunov 2^{nd} method for linear systems in order for the system to be asymptotically stable it is a necessary and sufficient condition that for a given hermitian positive defined matrix $\mathbf{Q}$, it exist a hermitian positive defined matrix $\mathbf{P}$ such that the following relation is proved:

$$\mathbf{A}^*\mathbf{P} + \mathbf{PA} = -\mathbf{Q} \tag{49}$$

where $\mathbf{A}^*$ corresponds to the conjugate transpose of $\mathbf{A}$.

Since for the imposed conditions there is no matrix $\mathbf{P}$ that for any $\mathbf{Q}$ positive defined is positive defined as well, stability cannot be proved by Lyapunov 2^o method for linear systems. This will be the subject of further work.

3.3. Control problem

By use of *Matlab* and more specifically *Simulink* the loop was closed and a *PID(s)* controller was implemented after a fine tune. For the controlled system, the desired characteristics of the time response were, M_p (maximum overshoot) ≤ 0.2 and $t_s[2\%]$ (settling time) ≤ 10s.

From (36), (37) and (45) it is clear the following block diagram describing the controlled system developed, as depicted in Fig. 7.

The controller specifications that verify the desired characteristics of the time response are given by:

$$P = 0.0084, \quad I = 0.0033, \quad D = 0.0047, \quad N = 67.64 \tag{50}$$

The global TF of the proposed Model for the closed control loop is given by:

$$CL = \frac{TF2^2\ G(s)}{1 + TF2^2\ G(s)} \tag{51}$$

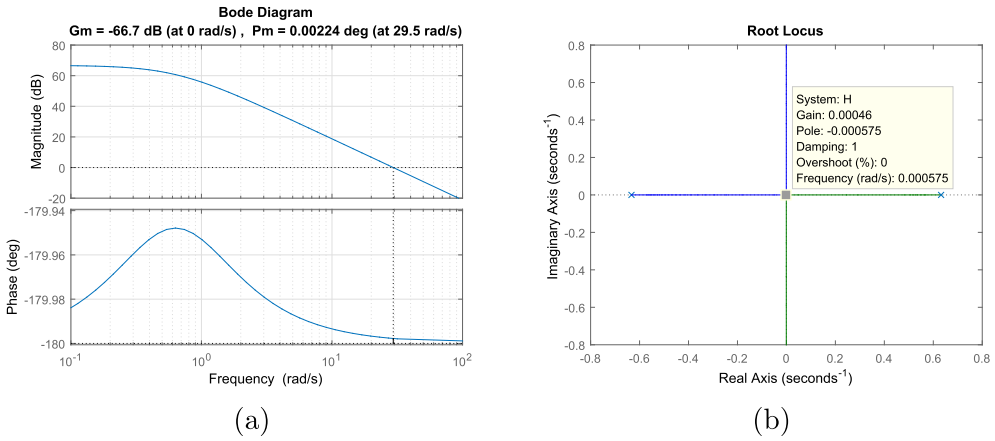

(a) (b)

Fig. 6. a) 2nd Order Model Open Loop System: Bode analysis. b) 2nd Order Model Open Loop System: Root locus analysis.

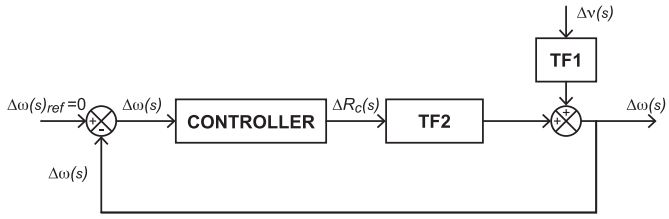

Fig. 7. Controlled system block diagram.

3.4. LQR controller design in continuous time-infinite horizon

In order to Design an Optimal Control Solution the problem is solved for infinite time, being therefore a sub-optimal controller. For that achievement it is required to define some steps. The control law is given by:

$$\mathbf{u} = -\mathbf{K}\,\mathbf{x} \tag{53}$$

$$CL = \frac{283.51\,s\,(s+67.64)\,(s+1.163)\,(s+0.633)\,(s+0.588)\,(s-0.6319)}{s\,(s+67.64)\,(s+63.28)\,(s-0.633)\,(s+0.5986)\,(s+0.6319)\,(s^2+3.76s+5.119)} \tag{52}$$

Some mathematical models will have infinite gain/phase margins. Of course no real-physical system has infinite margins but this will be an indication that the real-physical system has large margins. Infinite gain margin implies that a stable system is inherently stable for higher gains.

The *Root Locus* and *Bode* analysis is performed and shown in Fig. 8.

3.4.1. Performance index

The performance index is given by:

$$J = \int_{t_0}^{t_f} \left[\mathbf{x}^T(t)\mathbf{Q}\mathbf{x}(t) + \mathbf{u}^T(t)\mathbf{R}\mathbf{u}(t)\right] dt \tag{54}$$

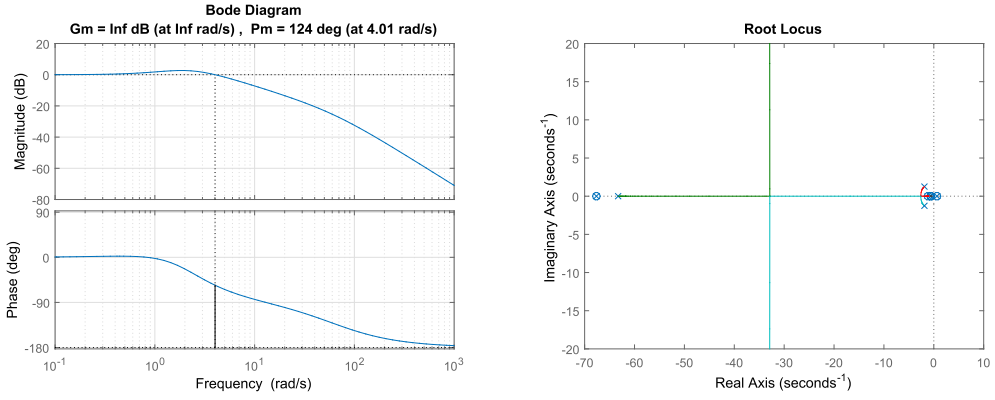

(a) (b)

Fig. 8. a) PID controlled system analysis: Bode analysis. b) PID controlled system analysis: Root locus analysis.

3.4.2. Weight matrices definition

For the state space matrices the values are tuned by performing several experiments to the model implemented on *Simulink*. Since **R** is related to the cost of energy, a higher **R** corresponds to a smaller gain, minimizing the energetic cost of the actuation. **Q** is related to how well do we want a state to follow a reference by minimizing the mean state error between the reference itself and the actual state.

3.4.3. Second-order model

The **Q** and **R** matrix for the second order model are given by:

$$\mathbf{Q} = \begin{bmatrix} 5 & 0 \\ 0 & 1 \end{bmatrix} \quad and \quad \mathbf{R} = [1] \tag{55}$$

The Riccati's algebraic equation is given by:

$$\mathbf{A}^T\mathbf{P} + \mathbf{PA} - \mathbf{PBR}^{-1}\mathbf{B}^T + \mathbf{Q} = 0 \tag{56}$$

where, **K** is given by:

$$\mathbf{K} = \mathbf{R}^{-1}\mathbf{B}^T\mathbf{P} \tag{57}$$

The LQR controller gains for the second order model are given by:

$$\mathbf{K} = [2.24 \quad -1.54] \tag{58}$$

3.5. Control problem

In this subsection the simplified model is used and simulated to have a grasp on the control strategy intended to implement. Although it is a model with reduced complexity since it does not include the dynamics associated with δi_d, the expected behavior is similar and therefore of interest.

After executing the process required to obtain the LQR controller, it is possible to study the systems behavior, performing a comparison to the system controlled by the PID controller, with the tuned specifications.

The following subsections display behaviors of both controllers previously studied, that is, the LQR and the PID controllers. The simultaneous display intends to ease the observation of the main differences between both controllers.

In a first stage analysis, wind speed is considered on its nominal value, 6 m/s, not taking into account the harmonic oscillations present in the real signal. This allows a clear analysis of the controller behavior. For all simulations made in *Simulink* the output variable shown is $\delta\omega$ (angular speed variation) and the control signal is δR_c (circuit resistance variation). The wind perturbation is expressed as $\delta v = 4\text{m/s}$ at $t = 10\text{s}$.

For the power coefficient variation analysis it is clear that the immediate wind speed increase is followed by a instant reduction of TSR resulting in a power loss and therefore a smaller power coefficient C_p. Such reduction in the TSR can only be contradicted by an increase of angular speed, which occurs by regulating the circuits resistance, which affects the passing current that affects the electromagnetic torque resulting in a change of angular speed. These objectives are represented in Fig. 9.

The variable speed wind system in study was simulated using Matlab/Simulink. The integration method used for solving the state equations of the system is Runge-Kutta of 4th order of integration, this method allows integration time steps of low amplitude, allowing for high precision results. This method is simple, robust and recognized has a good generic method for integrating equations.

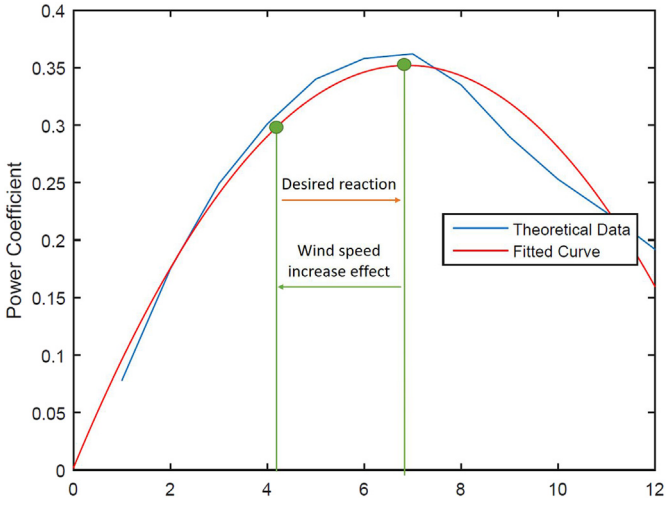

Fig. 9. Power vs wind speed with control.

3.5.1. Linear model

In this section the system is disturbed by an increase in wind speed that takes the form of a step input. It is important to notice that such disturbances are not observable in the wind behavior, it either takes the form of a ramp or of a more complex input. However for controller analysis purposes a step is valid since it represents the most abrupt way a disturbance can act on a system, since it is valid to conclude that the controller behaves accordingly to a step input, the reaction to a less abrupt change will be of higher quality.

Since linearizing non linear equations produces linear equations for the variables perturbation, the reference for the state variable $\delta\omega$ to follow is given by:

$$\delta\omega_{ref} = \omega_{opt}(t) - \omega_{opt}(o) \tag{59}$$

The simulation results of the angular speed variation and the TSR variation with the wind speed increase are shown in Fig. 10.

Although the LQR controller does not present overshoot, the settling time is considerably bigger when compared to the PID controller, but for the problem at hand does not present any inconvenience. The simulation results of the circuit resistance variation (input) and the i_q variation with the wind speed increase are shown in Fig. 11.

Although not clearly visible, after the wind speed increase at $t = 10\text{s}$ and the respective system time response, when at steady state there are slight differences in δR_c and i_q shown for the PID and LQR controller respectively in Tables 2 and 3.

In order to evaluate both controllers, input variations were set to have approximately the same range of actuation to understand how well the controller is appropriate to cause the desired effect in the turbines angular speed. The simulation results of the angular speed variation and the circuit resistance variation with the wind speed increase are shown in Fig. 12.

3.5.2. Non-linear model

In this subsection a comparison between controllers in the non linear models is shown the second order model. The simulation results of the non linear model for the angular speed variation and the TSR variation with the wind speed increase are shown in Fig. 13.

Here, it is clear that the LQR controller allows a better performance of the system, showing less overshoot and a smaller settling

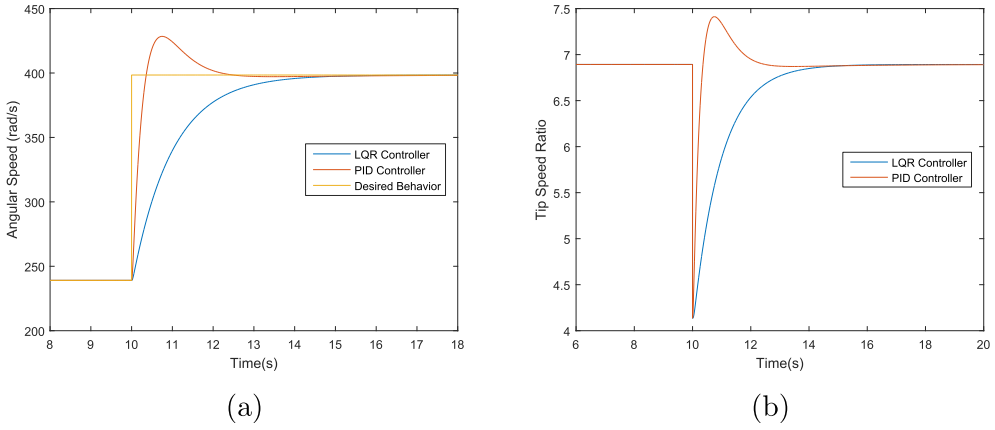

Fig. 10. a) Linear Model: Angular speed behavior. b) Linear Model: TSR variation.

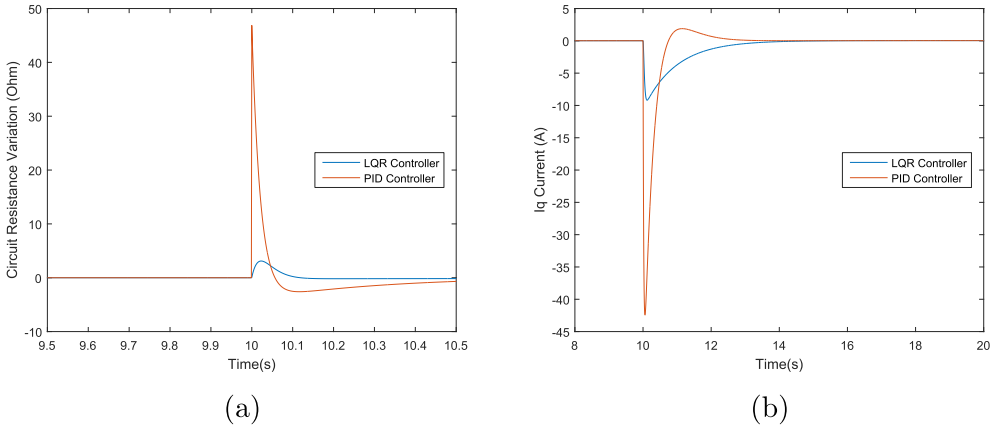

Fig. 11. a) Linear Model: Circuit resistance variation. b) Linear Model: Iq current behavior.

Table 2
PID Controller System Parameters variation, δR_c and i_q, due to wind speed increase.

Wind regime	$t < 10$ s	$t > 10$ s
δR_c (Ω)	0	0
i_q (A)	0.0169	0.039

Table 3
LQR Controller System Parameters variation, δR_c and i_q, due to wind speed increase.

Wind regime	$t < 10$ s	$t > 10$ s
δR_c (Ω)	0	− 0.089
i_q (A)	0.0169	0.039

time. In the initial moments the PID controller takes a few seconds to achieve the nominal value. The specifications regarding maximum overshoot and settling time are achieved for both controllers. It's clear that the LQR controller in order to have a better response requires higher variations of input (δR_c). The simulation results of the circuit resistance variation (input) and the i_q variation with the wind speed increase are shown in Fig. 14.

Although not clearly visible, after the wind speed increase at $t =$ 10s and the respective system time response, when at steady state there are slight differences in δR_c and i_q shown for the PID and LQR controller respectively in Tables 4 and 5.

4. Experimental setup

In this section experimental studies are presented with the objective of identifying the parameters of the developed model (see Table 6). The prototype and the accessories are shown in Fig. 4.

The VAWT prototype experiments were preformed in the wind tunnel at Mechanical Department, Instituto Superior Técnico, Universidade de Lisboa, Portugal. Both VAWT prototype and PMSG specifications are shown in Table 1.

The angular speed sensor works through a infrared sensor that consists in a high intensity LED diode and a photoelectric infrared cell developed in Ref. [4]. Obstacles passing between the LED diode and the photoelectric cell produces an interruption of the circuit, therefore between two consecutive interruptions a full lap is performed by the turbine.

The prototype, the anemometer and the angular speed sensor in the wind tunnel are shown in Fig. 15. This figure also shows a pitot tube that was used for measuring the wind speed.

In order to estimate the parameters present in the linear dynamic model proposed, different experiments were performed, to evaluate the turbine response to each input at a time and simultaneously. Exploiting the superposition of linear models, both input variables were used for the determination of the state space model. Multiple experiments are performed in order to improve the quality of the results.

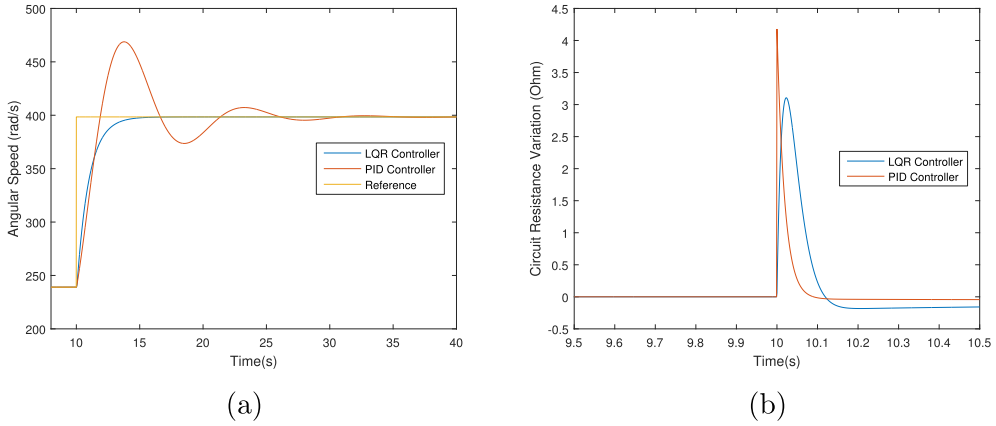

Fig. 12. a) Linear Model: Angular speed variation. b) Linear Model: Rc variation.

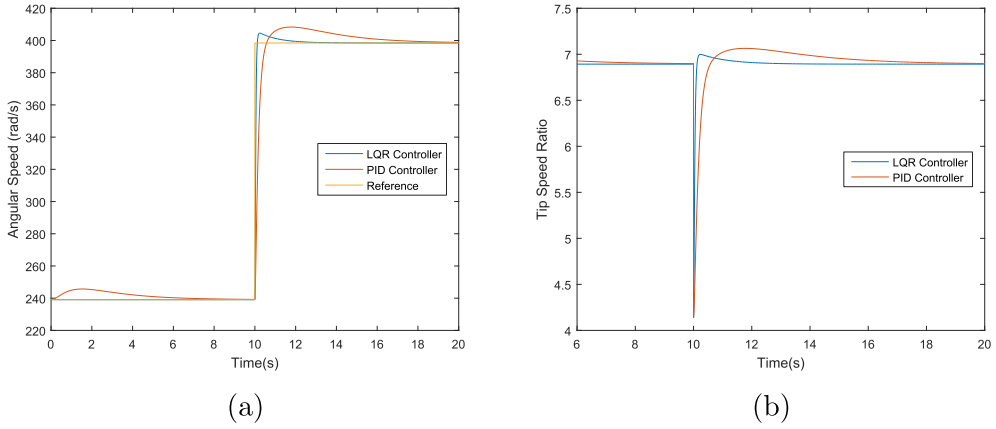

Fig. 13. a) Non-Linear Model: Angular speed variation. b) Non-Linear Model: TSR variation.

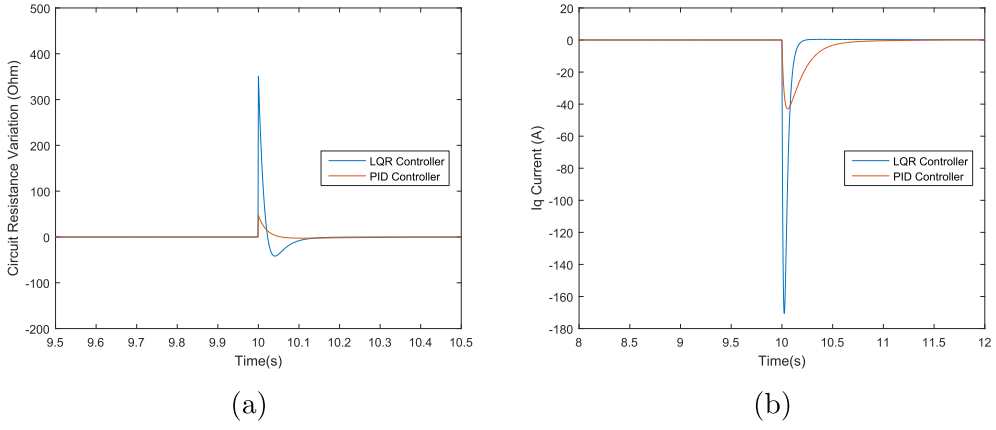

Fig. 14. a) Non-Linear Model: Circuit resistance variation. b) Non-Linear Model: Iq current behavior.

Table 4
PID Controller System Parameters variation, δR_c and i_q, due to wind speed increase.

Wind regime	$t < 10$ s	$t > 10$ s
δR_c (Ω)	− 0.06	− 0.0892
i_q (A)	0.0169	0.0468

Table 5
LQR Controller System Parameters variation, δR_c and i_q, due to wind speed increase.

Wind regime	$t < 10$ s	$t > 10$ s
δR_c (Ω)	− 0.06	− 0.0892
i_q (A)	0.0169	0.0468

Table 6
Assumed experimental conditions.

Parameters	Units	Value
Air Temperature	K	293.15
Air Density	kg/m^3	1.19
Gravitational Acceleration	m/s^2	9.8
Atmospheric Pressure	Pa	100606

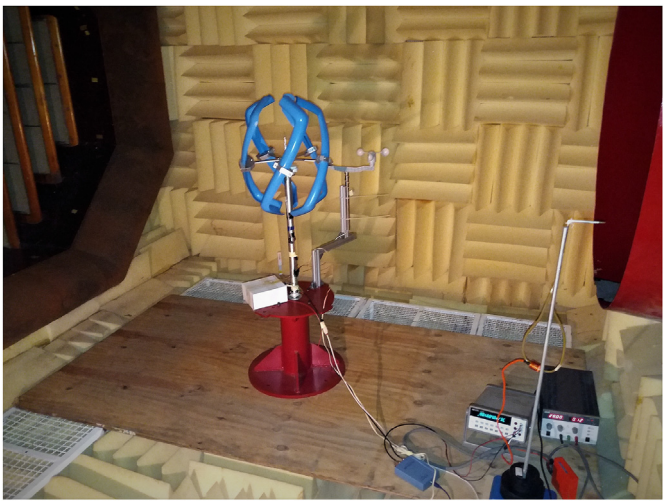

Fig. 15. Aeroacoustic wind tunnel Setup. Prototype and pitot tube installation.

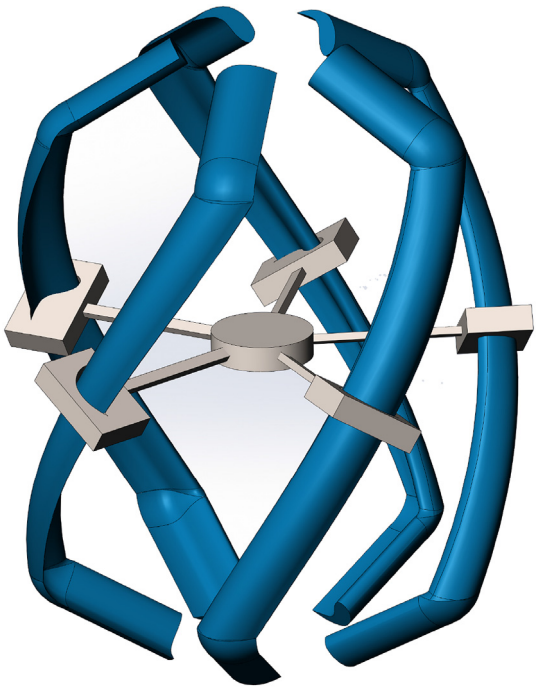

Fig. 16. VAWT 3D CAD model.

4.1. Inertial moment determination

Using a well known mass (M), and letting it fall by action of gravity (g) for a predefined distance (y) and measuring the time it takes to do so, knowing the diameter (d) where the cable is rolled, it is possible to determine an approximate value of J_t by simply applying equation (35).

Several weights were used and for each mass, 6 rehearsals were accomplished, to obtain an average time of descend. Since the VAWT prototype does not allow for a string winding completely circular, there are a slight deviations in descend speed due to the variance of distance from the string actuation to the rotating axis.

An example for the assembly required for the experiment is presented in Fig. 5. For the prototype developed after data analysis of the experiment it was possible to retrieve the value of the inertial moment, being 0.0913 kg m^2, approximately (see Table 7)0.1 kg m^2.

From the finite element method applied to the VAWT prototype CAD model, as shown in Fig. 16, the predicted moment of inertia is 0.0856 kg m^2, as shown in Fig. 17.

The standard variance of inertial moment test is large. Note that for identification purposes and for control purposes respectively, robustness due to the projection methods used or to the robustness inherent to the control technique used (LQR), the uncertainty on this parameter has little or no impact on the final result obtained. Moreover there are techniques that we plan to use in the future where this parameter is estimated during operation, such as Multiple-Model Adaptive Estimation (MMAE) or Robust Multiple Model Adaptive Control (RMMAC) [20].

Table 7
Inertial moment determination experiment.

J_t Determination	1	2	3	4	5
Mass(kg)	31.25	29.02	18.36	11.54	7.92
Average time(s)	3.66	3.8	5.48	8.12	9.35
I(kg m^2)	0.067	0.067	0.088	0.123	0.112
Average I(kg m^2)			0.0913		
Deviation	0.025	0.025	0.003	− 0.031	− 0.02
Variance			0.0005		
StandartDeviation			0.023		

4.2. Experimental data and parameters identification with potentiometers

All data obtained, namely, voltage and wind speed (pitot tube) were read from the *PicoScope* 6000 series, that was operating at a sample frequency of 151 Hz.

For these experiments a relay board was used in order to switch between three distinct circuit resistance states, respectively A, B and C. For state A, 3 potentiometers were installed allowing to study the systems behavior for multiple values of circuit resistance. For state B and C a specific value of circuit resistance was imposed, respectively 5 Ω and 2.5 Ω. Since the potentiometers tune was performed one at a time, the procedure consisted in varying from condition A for a specific value of resistance in the 3 potentiometers to state B and while in that condition the potentiometers were set to another value of resistive load, allowing for an off line tune not affecting the system. The scheme describing the assembled circuit is shown in Fig. 18.

This experiment data set consists in four distinct stages, as shown in Table 8.

This procedure intends to improve the quality of the identification performed, forcing the system to behave accordingly, that is, identifying a systems that complements all sorts of input variation, including when both inputs vary simultaneously.

From Fig. 19 it is clear the different effects of both inputs variation. The change in the circuit resistance produces quicker reactions of the voltage produced. This happens not only because of

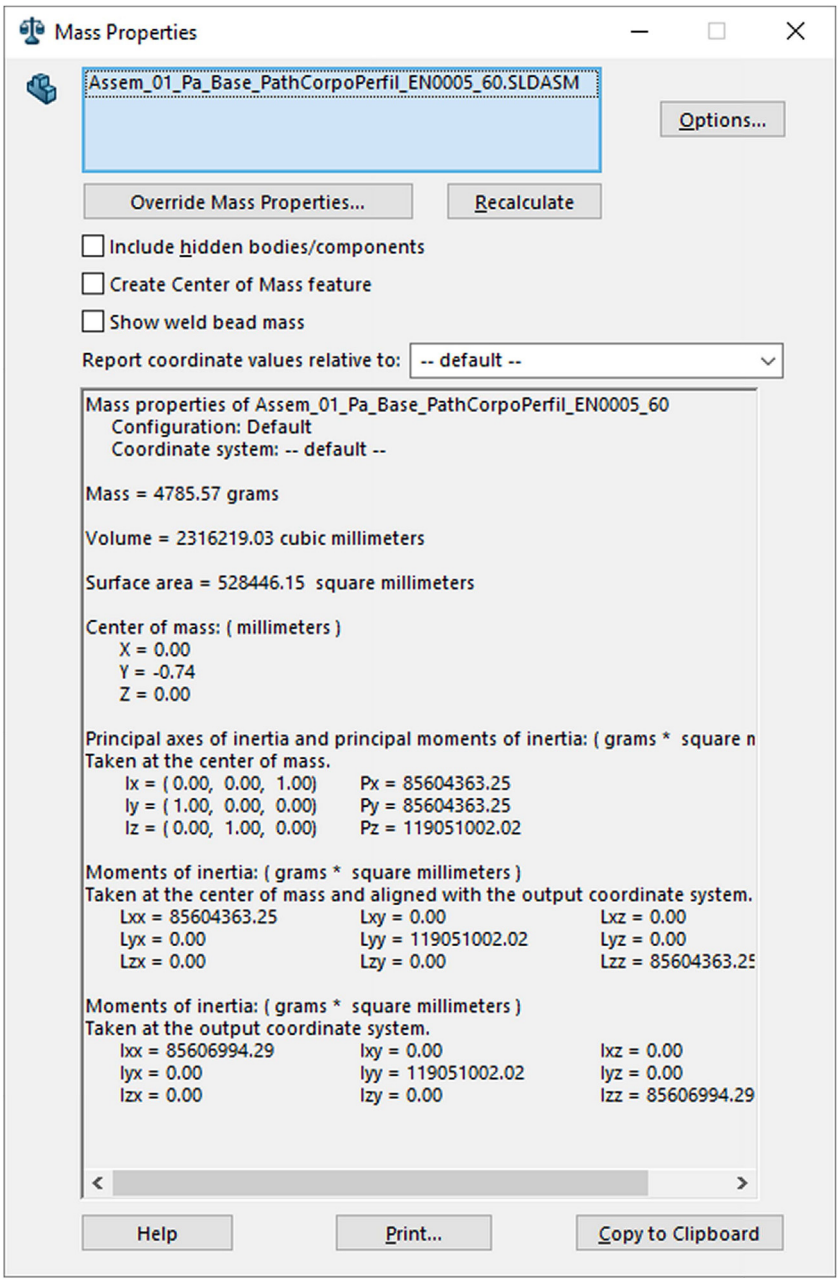

Fig. 17. Moment of inertia computed from CAD 3D model.

the fast electric dynamics but also because the change of resistance acts as a step being much more abrupt than the wind speed changes. Actually, when acting on the wind turbine the wind speed variation is not immediately evident at the voltage at the generator terminals. This is due to the moment of inertia that produces a slow dynamic between both variables. The angular speed variation throughout this experiments is shown in Fig. 20.

The wind speed variation throughout the experiment is shown in Fig. 21 where firstly the outliers were removed and then a low pass filter was applied to remove high frequency noise, due to minor turbulence effects and noise.

4.2.1. Multiple input single output identification analysis

Both inputs, wind speed and circuit resistance, together with the output are shown in Fig. 22.

4.2.1.1. Free matrix entries. The identified model with fixed rank ($n = 2$) and total parameter freedom produces an output that as a fitting with the measured output of 85.26%, presented in Fig. 23.

The developed second order model is given by:

$$\mathbf{A} = \begin{bmatrix} bJ^{-1} & -eJ^{-1} \\ d & 0 \end{bmatrix}, \quad \mathbf{B} = \begin{bmatrix} 0 \\ c \end{bmatrix}, \quad \mathbf{E} = \begin{bmatrix} aJ^{-1} \\ 0 \end{bmatrix} \tag{60}$$

$$\mathbf{C} = [1 \quad 0], \quad \mathbf{D} = [0] \tag{61}$$

The state space model generated by the identification method for the second order model is given by:

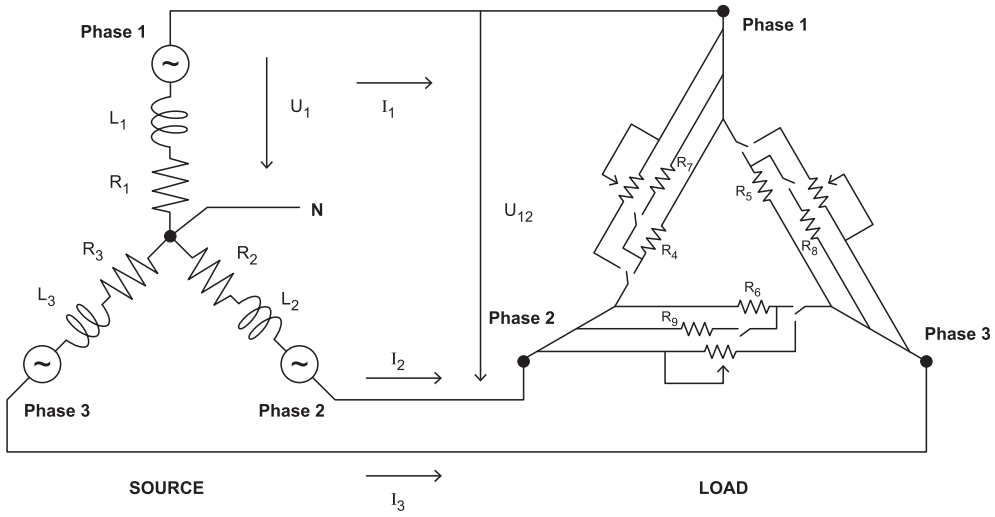

Fig. 18. Full circuit scheme with simplified load.

Table 8
Experimental data set stages.

Only the wind speed variation input is tested (δv)	$20 < t < 320$
Only the circuit resistance variation is tested (δR_c)	$320 < t < 500$
Wind speed is in steady state and resistors constant	$500 < t < 620$
Both inputs are varied simultaneously	$620 < t < 700$

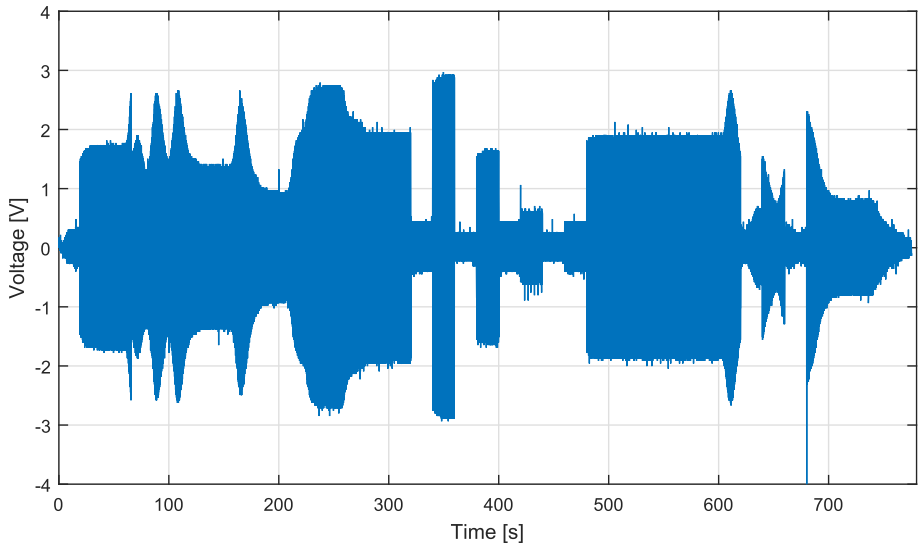

Fig. 19. Voltage at PMSG terminals.

$$\mathbf{A} = \begin{bmatrix} -1.32 \times 10^4 & -44.32 \\ -28.77 & -0.2376 \end{bmatrix}, \quad \mathbf{B} = \begin{bmatrix} 952 \\ 3.718 \end{bmatrix}, \quad \mathbf{E} = \begin{bmatrix} 7131 \\ -26.75 \end{bmatrix} \tag{62}$$

$$\mathbf{C} = [1 \quad 0], \quad \mathbf{D} = [0 \quad 0] \tag{63}$$

For this identified model, by evaluating the B matrix, knowing that $u = [\delta R_c]$, it is noticeable that the model predicts a important influence of δR_c since the actuation gains are high. However there still is a considerable discrepancy between the parameters values in the identified model and the theoretical, which might imply that some non linear disturbances occur in the functioning wind power system. The theoretical model, for the present operating conditions is given by:

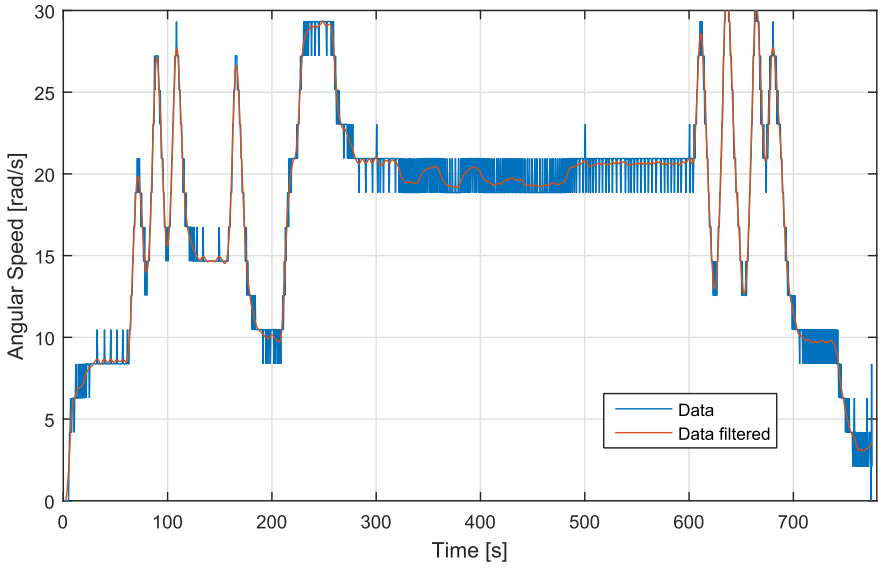

Fig. 20. Angular speed variation.

$$\mathbf{A} = \begin{bmatrix} -5 \times 10^{-3} & -24.48 \\ -0.4733 & 0 \end{bmatrix}, \quad \mathbf{B} = \begin{bmatrix} 0 \\ -1.336 \end{bmatrix}, \quad \mathbf{E} = \begin{bmatrix} 0.169 \\ 0 \end{bmatrix} \tag{64}$$

$$\mathbf{C} = [1 \quad 0], \quad \mathbf{D} = [0] \tag{65}$$

5. Conclusion

In this work, the modeling of a wind turbine power system is

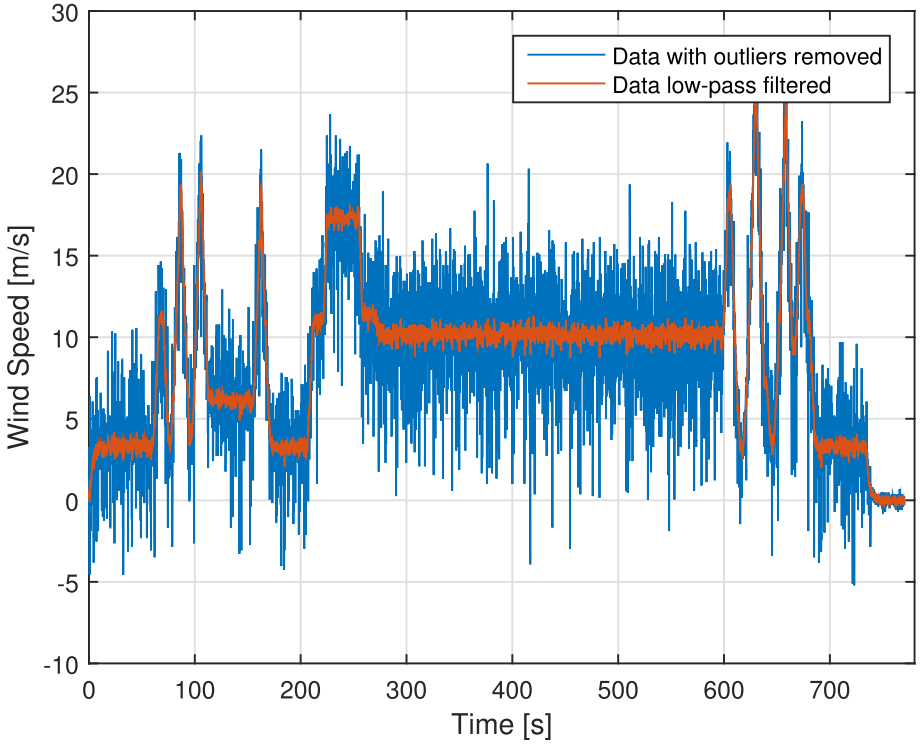

Fig. 21. Wind speed variation.

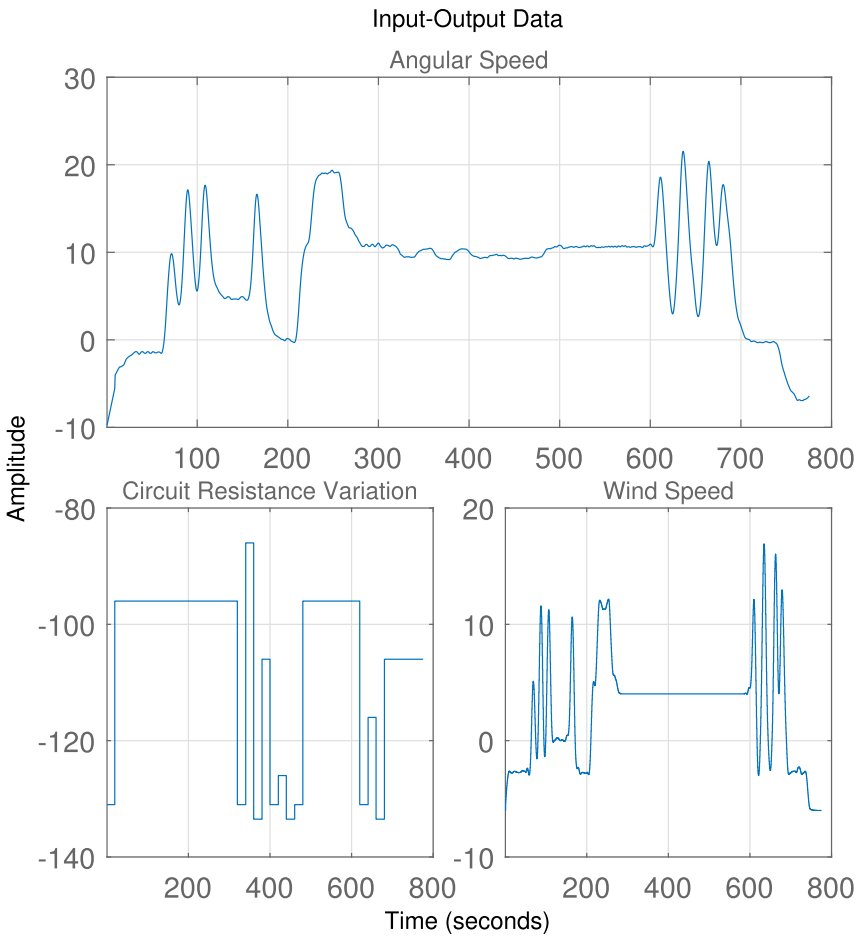

Fig. 22. Data set for MISO identification.

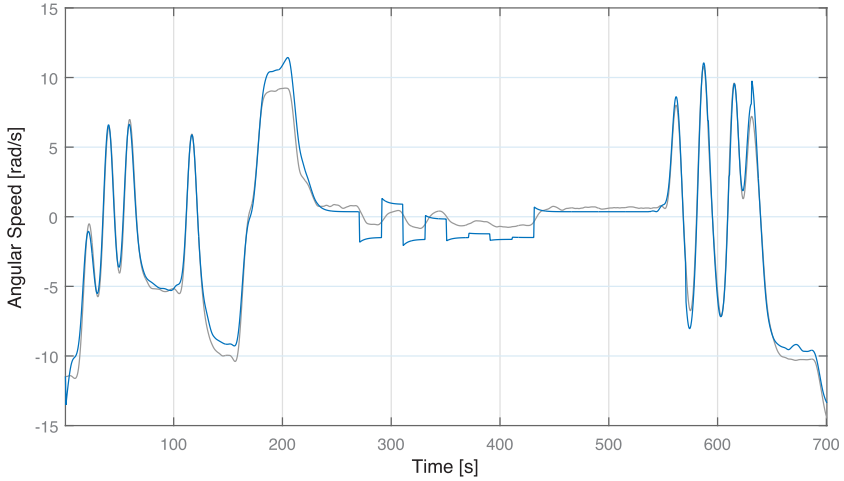

Fig. 23. Model comparison for MISO system: (Second-Order Model).

developed and validated with identified models obtained from experimental data analysis from the Darrieus prototype developed.

For a model with the same rank as the theoretical model but total parameter freedom, the result between the outcome of the model and the identified one produces a fitting of 85%, which is reasonable good.

An LQR controller was developed for control and the simulations were performed to verify its performance. The results from the simulations show that a high resolution, wide range and quick dynamic actuator is required, which is consistent with the conclusions of the analysis performed on the model obtained from the identification experiment.

Acknowledgments

This work is funded by Portuguese Funds through the Foundation for Science and Technology FCT under the project LAETA 2015–2020, reference UID/EMS/50022/2013.

References

[1] Gomes ILR, Pousinho HMI, Melcio R, Mendes VMF. Stochastic coordination of joint wind and photovoltaic systems with energy storage in day-ahead market. Energy April 2017;124:310–20.
[2] Cheng M, Zhu Y. The state of the art of wind energy conversion systems and technologies: a review. Energy Convers Manag December 2014;88:332–47.
[3] Kandpal TC, Broman L. Renewable energy education: a global status review. Renew Sustain Energy Rev June 2014;34:300–24.
[4] Batista NC, Melicio R, Matias JCO, Catalão JPS. New blade profile for Darrieus wind turbines capable to self-start. In: Proceedings of the renewable power generation conference; 05-08 September 2011. p. 1–5. Edinburgh, UK.
[5] Abdalrahman G, Melek W, Lien F-S. Pitch angle control for a small-scale Darrieus vertical axis wind turbine with straight blades (H-type VAWT). Energy December 2017;114(Part B):1353–62.
[6] Batista NC, Melicio R, Mendes VMF, Calderón M, Ramiro A. On a self-start Darrieus wind turbine: blade design and field tests. Renew Sustain Energy Rev December 2015;52:508–22.
[7] Batista NC, Melicio R, Matias JCO, Catalo JPS. Self-start evaluation in lift-type vertical axis wind turbines: methodology and computational tool applied to asymmetrical airfoils. In: Proceedings of the III international conference on power engineering, energy and electrical drives (PowerEng 2011); May 2011. p. 16. Malaga, Spain, 1113.
[8] Ma N, Lei H, Han Z, Zhou D, Bao Y, Zhang K, Zhou L, Chen C. Airfoil optimization to improve power performance of a high-solidity vertical axis wind turbine at a moderate tip speed ratio. Energy May 2018;150:236–52.
[9] Melicio R, Mendes VMF, Catalão JPS. A pitch control malfunction analysis for wind turbines with permanent magnet synchronous generator and full-power converters. Elec Power Compon Syst January 2010;38(4):387–406.
[10] Melicio R, Mendes VMF, Catalão JPS. Comparative study of power converter topologies and control strategies for the harmonic performance of variable-speed wind turbine generator systems. Energy January 2011;36(1):520–9.
[11] Boukhezzar B, Lupu L, Siguerdidjane H, Hand M. Multivariable control strategy for variable speed, variable pitch wind turbines. Renew Energy July 2007;32(8):1273–87.
[12] Marques T. Control and operation of a vertical axis wind turbine. Masters Thesis. Lund University; June 2014.
[13] González LG, Figueres E, Garcerá G, Carranza O. Dynamic response analysis of small wind energy conversion systems (WECS) operating with torque control versus speed control. In: International conference on renewable energies and power quality; 15-17 April 2009. p. 437–41. Valencia, Spain.
[14] Rezaeiha A, Kalkman I, Blocken B. Effect of pitch angle on power performance and aerodynamics of a vertical axis wind turbine. Appl Energy July 2017;197:132150.
[15] Perera LP, Oliveira P, Soares CG. System identification of nonlinear vessel steering. J Offshore Mech Arctic Eng June 2015;137(3):1–7.
[16] Pagnini LC, Burlando M, Repetto MP. Experimental power curve of small-size wind turbines in turbulent urban environment. Appl Energy September 2015;154:112–21.
[17] Zhou K, Doyle JC, Glover K. Robust and optimal control. New Jersey, USA: Prentice hall; 1996.
[18] Patil K, Mehta B. Modeling and control of variable speed wind turbine with permanent magnet synchronous generator. In: International conference on advances in green energy; 17-18 December 2014. p. 258–64. Thiruvananthapuram, India.
[19] Paraschivoiu I. Wind turbine design with emphasis on Darrieus concept. first ed. Canada: Polytechnic International Press; 2002.
[20] Sajjad F, Athans M, Pascoal A. Issues, progress and new results in robust adaptive control. Int J Adapt Contr Signal Process December 2006;20(10):519–79.